



Superior performance of FeVO₄@CeO₂ uniform core-shell nanostructures in heterogeneous Fenton-sonophotocatalytic degradation of 4-nitrophenol



Gh. Eshaq^{a,b,*}, Shaobin Wang^c, Hongqi Sun^d, Mika Sillanpää^a

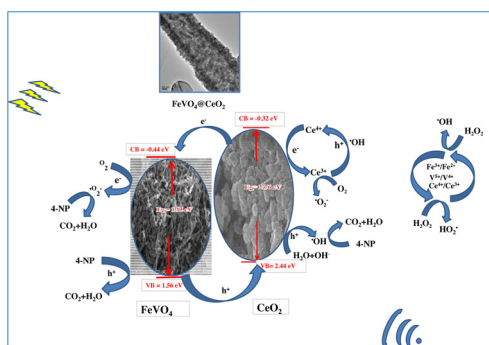
^a Department of Green Chemistry (DGC), School of Engineering Science, Lappeenranta University of Technology, Sammonkatu 12, FI-50130, Mikkeli, Finland

^b Petrochemicals department, Egyptian Petroleum Research Institute, Nasr City, Cairo 11727, Egypt

^c School of Chemical Engineering, The University of Adelaide, Adelaide, SA 5005, Australia

^d School of Engineering, Edith Cowan University, Perth, WA 6027, Australia

GRAPHICAL ABSTRACT



ARTICLE INFO

Editor: Xiaohong Guan

Keywords:

Core/shell

Sonophotocatalysis

Synergy index

Semiconductor

4-nitrophenol

ABSTRACT

Porous FeVO₄ nanorods decorated on CeO₂ nanocubes (FeVO₄@CeO₂) were successfully prepared via a facile hydrothermal route and tested in the degradation of 4-nitrophenol (4-NP) for enhanced heterogeneous oxidation using ultrasonic (US), ultraviolet (UV), and binary irradiation US/UV, respectively. The nanostructure of the core-shell FeVO₄@CeO₂ was characterised using XRD, SEM, EDS elemental mapping, TEM, HRTEM, SAED, FTIR, Raman, BET, point of zero charge (PZC), XPS analysis and UV-vis DRS. The effect of various parameters, for examples, nanostructured core-shell amounts, hydrogen peroxide concentration, initial concentration, pH and irradiation time, on 4-NP degradation were investigated for the optimisation of the catalytic performance. The durability and stability of the core-shell nanostructured materials were also investigated and the obtained results revealed that the catalysts can endure the harsh sonophotocatalytic conditions even after six cycles. Mineralisation experiments were investigated using the optimised parameters. The core-shell nanostructured FeVO₄@CeO₂ has higher PZC than pure FeVO₄ and CeO₂, leading to excellent sonophotocatalytic activity even at high pH and stability for the degradation of 4-NP after six cycles. A possible mechanism over the FeVO₄@CeO₂ was proposed based on the special three-way Fenton-like mechanism and the dissociation of H₂O₂ with the experiments of active species trapping and calculated band gap energy.

* Corresponding author.

E-mail address: gh.Eshaq@yahoo.com (G. Eshaq).

<https://doi.org/10.1016/j.jhazmat.2019.121059>

Received 13 May 2019; Received in revised form 14 August 2019; Accepted 20 August 2019

Available online 20 August 2019

0304-3894/ © 2019 Elsevier B.V. All rights reserved.

1. Introduction

Nitro aromatics have been widely used in the manufacture of many chemical products like pharmaceuticals, dyes, solvents, explosives and fungicidal agents (Herrera-Melián et al., 2012; Yehia et al., 2016). Nevertheless, these nitro compounds have serious effects on the environment and also a highly toxic effect on living organisms (Lunhong and Jing, 2013). Among these compounds, 4-nitrophenol (4-NP) is used as a chemical intermediate for rubber, lumber preservatives, azo and others (Peretz, 2019). According to the USA Environmental Protection Agency (EPA), 4-NP has been classified as a priority toxic pollutant (Mishra and Gogate, 2011). Advanced Oxidation Processes (AOPs), are considered as the most promising approaches to the destruction of recalcitrant organic pollutants, and are based on the generation of hydroxyl radicals (Erick et al., 2004). Recently, sonolysis with an appropriate catalyst has received great attention as a promising system owing to the generation of more free radicals (Ricardo and Efraim, 2018; Slimane et al., 2010).

Nevertheless, it has been observed that a combination of different AOPs has been found to be more efficient and foster the degree of mineralisation of organic pollutants (Gogate, 2008; Bagal and Gogate, 2014). It has been reported that the simultaneous use of sonolysis and photocatalysis called sonophotocatalysis can be considered a promising technique with increasing the production of $\cdot\text{OH}$ radicals (Chilukoti et al., 2011; Elshafei et al., 2018).

Nowadays, the core-shell nanostructure have great potential in catalysis because of their unique chemical and physical characteristics and have many advantages such as an increased number of surface-active sites for the core and promotion by the shell of catalytic activity (Zaleska et al., 2016; Mitsudome and Kaneda, 2013). Moreover, the reactions of all catalysts occur at the same time and the strength of the shell can protect the core and prevent assemblage of the particles (Zhang et al., 2014; Pham et al., 2018). In this context, many researchers have used various core shell nanostructures (Siadatnasab and Khataee, 2017; Shah et al., 2016; Pham and Kim, 2018; Khanchandani et al., 2016; Ding et al., 2016; Kanmani and Ramachandran, 2012; He et al., 2014; Habila et al., 2016; Zheng et al., 2018a; Huang et al., 2017; Hu et al., 2011; Li et al., 2015a; Khanchandani et al., 2014; Ghows and Entezari, 2012; Ijaz et al., 2016). Among the inorganic shell materials, cerium oxide (CeO_2) has served as one of the most efficient photocatalysts for the degradation of organic pollutants because of its ability to transform between Ce^{+3} and Ce^{+4} states at oxygen vacancy sites, and to facilitate electron transfer and e^-/h^+ pair diffusion between CeO_2 and another semiconductor such as Cu_2O (Chae et al., 2017), CdS (Zhang et al., 2017) and TiO_2 (Chen et al., 2017; Cargnello et al., 2010). Accordingly, the preparation of core-shell materials with a metal as a core and ceria as a shell is of great significance. Iron vanadate FeVO_4 is considered as a semiconducting, highly stable, selective as a photocatalyst according to its unique and excellent performance (Hosseinpour-Mashkani et al., 2016).

The aim of the current work is to investigate the combination of heterogeneous Fenton-like and sonophotocatalysis which is considered as another possible way to increase the generation of free radicals in the system. Whereas the use of heterogeneous Fenton-like with sonophotocatalysis plays an effective role in enhancing the extent of degradation with adjusting the parameter conditions in order to get more hydroxyl radical and maximum beneficial effects.

To the best of our knowledge, successful synthesis of a $\text{FeVO}_4/\text{CeO}_2$ core shell nanostructure and its use as heterogenous Fenton-like catalyst in the degradation of 4-NP in the presence of ultrasonic (US), ultraviolet (UV), and binary irradiation US/UV, using H_2O_2 as an oxidant have not been reported. In this work, a $\text{FeVO}_4/\text{CeO}_2$ was synthesized and investigated with XRD, SEM, EDS, TEM, HRTEM, SAED, FTIR, Raman, N_2 -adsorption-desorption, DRS and XPS. The different degradation parameters, for instance, irradiation time, catalyst loading, pH and H_2O_2 initial concentration were optimized, and the

mineralization and recyclability were examined. Moreover, the synergistic effect with reaction kinetics was investigated in detail and the possible mechanism was discussed.

2. Experimental

2.1. Catalysts preparation

2.1.1. Preparation of porous FeVO_4 nanorods

$\text{FeCl}_3 \cdot 6\text{H}_2\text{O}$ (2 mmol) was dissolved in 10 mL of deionised water and NH_4VO_3 (2 mmol) was dissolved in another 10 mL of deionised water at 90 °C. Next, NH_4VO_3 solution was slowly added to $\text{FeCl}_3 \cdot 6\text{H}_2\text{O}$ solution under constant stirring. After 20 min of stirring, the obtained slurry was placed in a 50 mL Teflon-lined stainless-steel autoclave. The autoclave was sealed and heated at 180 °C for 3 h and then left to cool down naturally to the ambient temperature. The obtained precipitate was separated by centrifugation, washed with deionised water and absolute ethanol several times, and then dried in an oven at 60 °C for 6 h. After drying, the obtained powder was calcined at 500 °C at a rate of 5 °C/min for 2 h (Kaneti et al., 2013).

2.1.2. Preparation of CeO_2 nanocubes

CeO_2 nanocubes were prepared using an ultrasonic-assisted precipitation method as described in (Krishnamoorthy et al., 2014a). $\text{Ce}(\text{NO}_3)_3 \cdot 6\text{H}_2\text{O}$ (0.1 M) and NaOH (0.3 M) solutions were prepared and the NaOH solution was added dropwise to the cerium nitrate solution under sonication. After that, the slurry was kept under sonication for 60 min. The obtained yellowish precipitates of cerium hydroxide were separated by centrifugation, washed with deionised water several times and then calcined at 250 °C for 4 h.

2.1.3. Preparation of $\text{FeVO}_4/\text{CeO}_2$ core shell nanostructures

$\text{FeVO}_4/\text{CeO}_2$ core shell nanostructures were prepared using a hydrothermal route, where 0.1 g of FeVO_4 as-prepared, 0.5 g of $\text{CO}(\text{NH}_2)_2$, 0.2 g of CeCl_3 , and 1.0 g (PVP, Mw = 58,000) were added to 80 mL of ethanol (50%, V/V) under continuous stirring for 6 h. The suspension was placed in a 50 mL Teflon-lined stainless-steel autoclave that was heated at 110 °C for 20 h and then left to cool down naturally to the ambient temperature. The obtained $\text{FeVO}_4/\text{CeO}_2$ was collected by centrifugation, washed several times in deionised water and absolute ethanol, dried in an oven at 50 °C for 12 h and then calcined at 500 °C for 4 h (Zheng et al., 2018b).

2.2. Characterisation

The crystalline phase was investigated by XRD analysis on a PANalytical diffractometer with $\text{Cu K}\alpha$ radiation (wave-length = 1.54 Å) operated at 40 kV and 40 mA. SEM with energy dispersive X-ray spectroscopy (HITACHI /EDS S-4800) attached was used. TEM, HRTEM and SAED were measured on a JEOL JEM-2010 (HT) operated at 200 kV. FTIR spectrum (Bruker Platinum ATR VERTEX 70) and Raman analysis were measured using a Horiba Jobin Yvon, and a Labram HR, respectively. Surface texture parameters (BET) were measured by nitrogen adsorption/desorption using a MicroActive-TriStar II Plus 2.03. The PZC was determined using the mass titration method (Franca et al., 2009). XPS was done on an ESCALAB 250Xi with Al-K (1486.6 eV). DRS was done on an Agilent Cary 5000 UV-vis spectrometer with a DRA 2500 integrating sphere.

2.3. Sonophotocatalytic reactor and experimental procedures

Ultrasonic experiments were performed in programmable sonication at an ultrasound frequency of 20 kHz (Sonics & Materials, Inc., VCX 750) with a titanium alloy probe with a tip diameter of 13 mm and maximum power output of 125 W. Water circulation was used to maintain the reaction temperature at 25 ± 2 °C. The quartz reactor

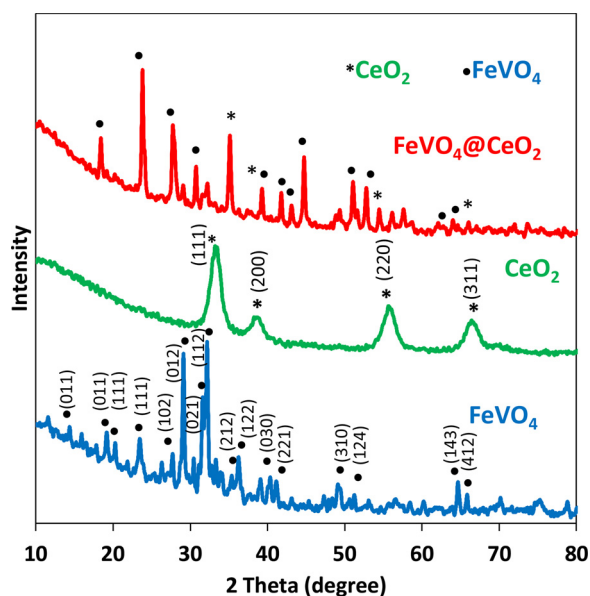


Fig. 1. XRD patterns of FeVO₄, CeO₂, and FeVO₄@CeO₂.

was filled with 110 mL 4-NP solution for each experiment, followed by a dispersed specific amount of the prepared catalyst to the solution. The reaction was initiated once adding H₂O₂. The obtained samples were analysed using an HPLC (SHIMADZU®) equipped with a Phenomenex® C18 column (5 μ m, 150 mm \times 4.6 mm) and a UV detector adjusted to 285 nm. A mixture of acetonitrile and Milli-Q water with a volumetric ratio of 50:50 was used as the mobile phase throughout the analysis with a flow rate of 1 mL min⁻¹. A Total Organic Carbon Analyzer (TOC-VCPH Shimadzu) equipped with an auto sampler (ASI-V Shimadzu).

3. Results and discussion

3.1. Characteristics of the prepared FeVO₄@CeO₂ core shell nanostructure

3.1.1. XRD

The crystalline phases and composition of pure FeVO₄, CeO₂ and FeVO₄@CeO₂ were determined by XRD analysis Fig. 1. The porous FeVO₄ nanorods present a similar XRD pattern to the triclinic FeVO₄ (JCPDS No. 71-1592). Further, CeO₂ prepared ultrasonically shows all the diffraction peaks matched very well with the nanocrystals of cubic fluorite structure (JCPDS No. 75-0390). The diffraction pattern of the FeVO₄@CeO₂ shows that all the peaks are in good agreement with the peaks of the triclinic structure of the FeVO₄ and of cubic CeO₂ nanoparticles. The decrease intensities in the diffraction peaks of FeVO₄ were observed as a result of CeO₂ coating. The average crystallite sizes calculated using the Scherrer equation of FeVO₄, CeO₂ and FeVO₄@CeO₂ are 45, 20 and 78 nm, respectively.

3.1.2. SEM - EDS with elemental mapping

To obtain insights into the morphology and surface features of the prepared samples, we carried out SEM analysis. Fig. 2(a-c) show the SEM of the individual FeVO₄, CeO₂ and FeVO₄@CeO₂ core shell nanostructure, respectively. Fig. 2a shows that the morphology of FeVO₄ is in porous nanorod-type with smooth surfaces. Fig. 2b shows that CeO₂ has a flower-like structure. The SEM image of FeVO₄@CeO₂ in Fig. 2c, shows the core-shell nanostructure, where the porous nanorod particles of FeVO₄ are shielded by a thin layer of CeO₂ particles. To confirm the core-shell nanostructure and the distribution of the elements in the core-shell nanostructure, Fig. 2(d-i) shows the EDX spectrum of FeVO₄@CeO₂ and EDS mapping.

3.1.3. TEM, HRTEM and SAED

Fig. 3 (a-c) show the TEM images of FeVO₄, CeO₂ and FeVO₄@CeO₂, respectively. The morphology of FeVO₄ shows porous nanorods with an average diameter of 45–50 nm, whereas CeO₂ is cube-shaped particle with an average size of 15–20 nm, which agrees with the data calculated by the Scherrer equation. Based on the TEM image, the shell thickness was determined to be 25 nm.

The corresponding SAED patterns of FeVO₄, CeO₂ and FeVO₄@CeO₂ in Fig. 3(d-f) endorse the presence of single crystalline phase of triclinic FeVO₄, cubic fluorite CeO₂ and their mixture. Fig. 3 (g) shows the HRTEM image of the heterojunction area between FeVO₄ and CeO₂ in FeVO₄@CeO₂, illustrating the presence of two sets of different interplanar spacing. The lattice fringes of 0.624 and 0.278 nm correspond to the interplanar spacing of (111) and (112) planes of triclinic FeVO₄ phase, respectively, while the interplanar spacing of 0.318 and 0.265 nm matches well with the fringe spacing of (111) and (200) lattice planes of the cubic fluorite CeO₂ structure, respectively.

3.1.4. FTIR

FTIR analysis for FeVO₄, CeO₂ and FeVO₄@CeO₂ was carried out and the obtained spectra are presented in Fig. 4. The bands at 3400 and 1630 cm⁻¹ are ascribed to the OH stretching vibrations of the absorbed water molecules. For FeVO₄, the bands appearing at 880 and 1050 cm⁻¹ are ascribed to the terminal V–O stretching vibrations. The presence of bands at 700–800 cm⁻¹ is an indication of the bridging V–O...Fe stretching vibration (Vuk et al., 2001) while those appearing at 550–700 cm⁻¹ are ascribed to mixed bridging V–O...Fe and V...O...Fe stretching. These data concur well with the previously published data (Nithya et al., 2011). The FTIR spectrum of CeO₂ exhibits a strong broad band at 550 cm⁻¹ ascribed to the stretching vibration of Ce–O (Ansari et al., 2009). It is clear that this band became broader in the FeVO₄@CeO₂ spectrum and can be ascribed to the overlapping between the V–O...Fe band and Ce–O band.

3.1.5. Raman

Further evidence of core shell formation in FeVO₄@CeO₂ nanostructures is revealed by Raman spectroscopy. The Raman spectra of FeVO₄, CeO₂ and FeVO₄@CeO₂ core shell nanostructures are shown in Fig. 5. The Raman spectrum of FeVO₄ shows the characteristic bands of FeVO₄, which revealed that the peaks between (970–895 cm⁻¹), are assigned to the terminal V–O stretching, and those appear at (890–736 cm⁻¹) corresponding to the bridging V–O–Fe stretching, while the peaks between (730–633 cm⁻¹) corresponding to the mixed bridging V–O–Fe and V–O–Fe stretching and the bands observed at (502–317 cm⁻¹) are attributed to V–O–V deformations and Fe–O stretching (Lehnen et al., 2014). In the case of the Raman spectrum of CeO₂ exhibit a sharp band at 463 cm⁻¹ is assigned to the F_{2g} modes of CeO₂, thus confirming the cubic fluorite structure (Fan et al., 2016). The Raman spectrum of FeVO₄@CeO₂ exhibits all the characteristic bands of FeVO₄ and CeO₂ with a slight decrease in the intensity of the bands assigned to FeVO₄, which can be attributed to the coverage of FeVO₄ nanoparticles with CeO₂ nanoparticles.

3.1.6. BET

Texture analysis of FeVO₄, CeO₂ and FeVO₄@CeO₂ were performed and the surface areas (S_{BET}) and total pore volumes (V_p) are listed in Table 1. The isotherms of all the catalysts Fig. 6 are of type IV with a hysteresis loop of type H3 (Sing et al., 1985), confirming that the pore size is mainly in the range of mesopore (Cao et al., 2012). As shown in Fig. 6 (inset) and Table 1, the pores of the catalysts are in good agreement with the mesoporous structure. The S_{BET} values of FeVO₄ and CeO₂ are 24.2 and 20.5 m² g⁻¹, respectively, while the value of FeVO₄@CeO₂ is 27.5 m² g⁻¹, larger than that of FeVO₄ and CeO₂. Moreover, FeVO₄@CeO₂ also displays nearly two times greater pore volume (0.062 cm³ g⁻¹) than FeVO₄ (0.032 cm³ g⁻¹) and CeO₂ 0.032 cm³ g⁻¹. The larger (S_{BET}) and (V_p) of FeVO₄@CeO₂ increase the

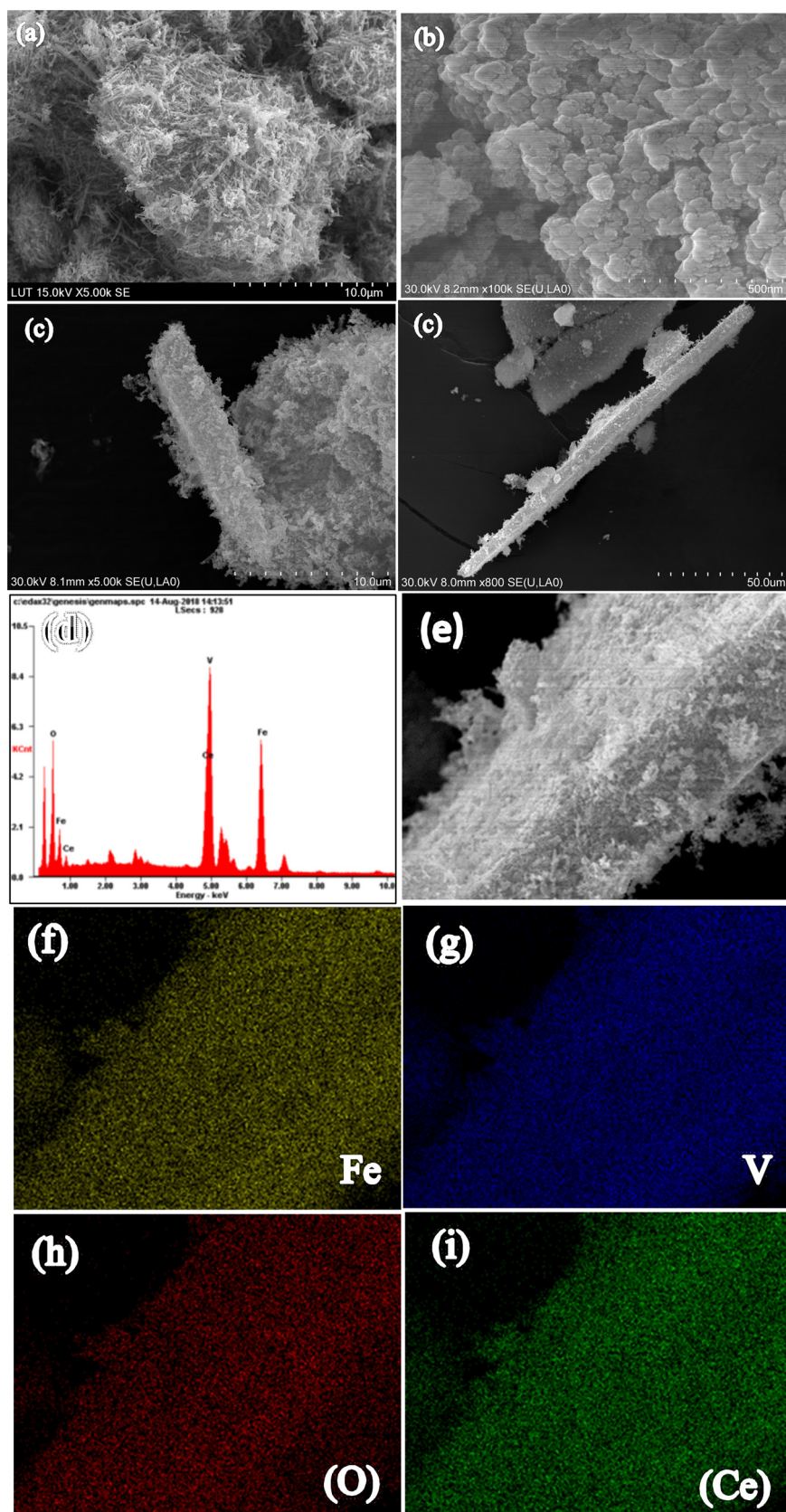


Fig. 2. SEM images of (a) FeVO₄, (b) CeO₂, and (c) FeVO₄@CeO₂ (d) EDS spectrum, (e) SEM image of FeVO₄@CeO₂, and EDS mapping of (f) Fe, (g) V, (h) O, (i) Ce element in FeVO₄@CeO₂.

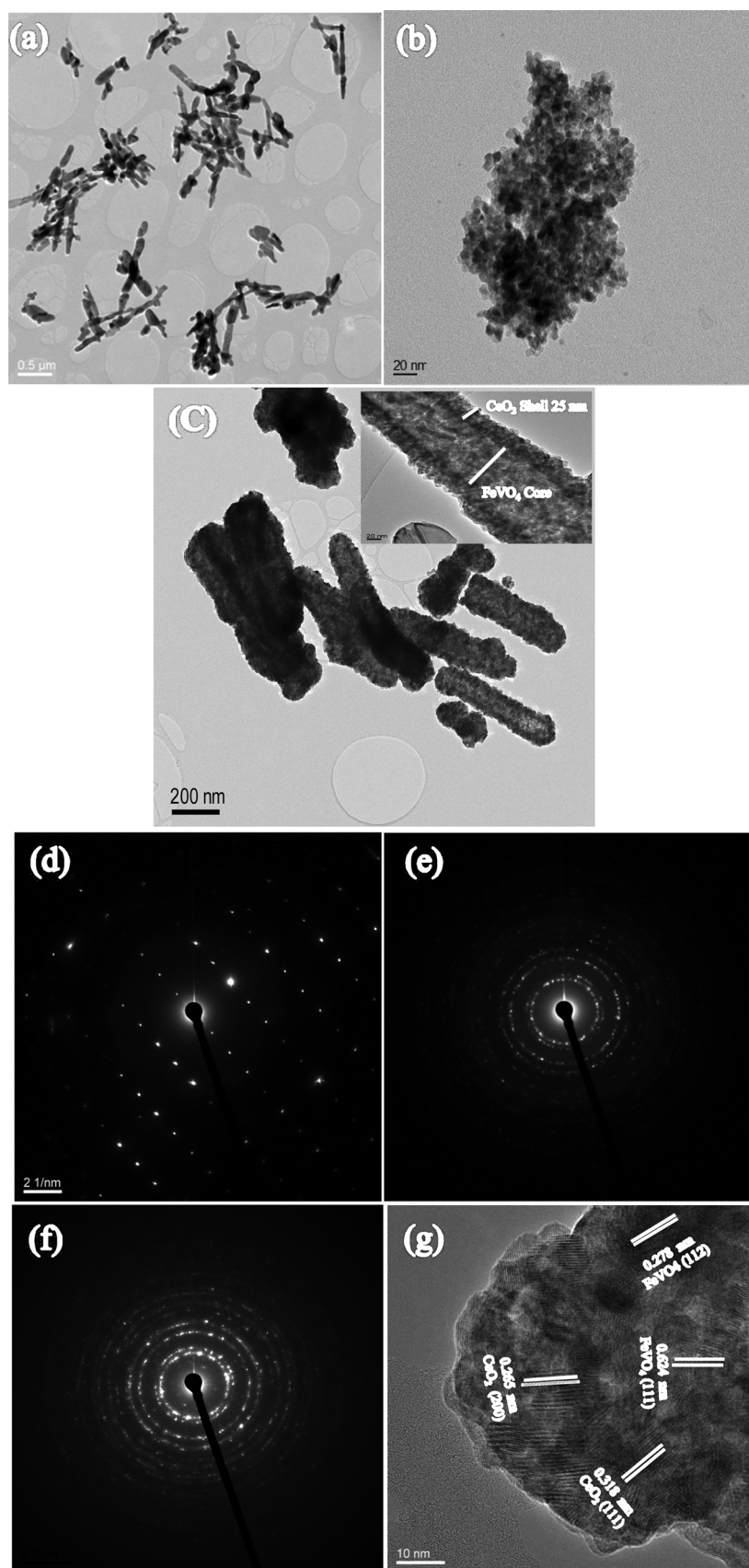


Fig. 3. TEM images of (a) FeVO_4 , (b) CeO_2 and (c) $\text{FeVO}_4@ \text{CeO}_2$, SAED images of (d) FeVO_4 , (e) CeO_2 , and (f) $\text{FeVO}_4@ \text{CeO}_2$ and HRTEM image (g) of $\text{FeVO}_4@ \text{CeO}_2$.

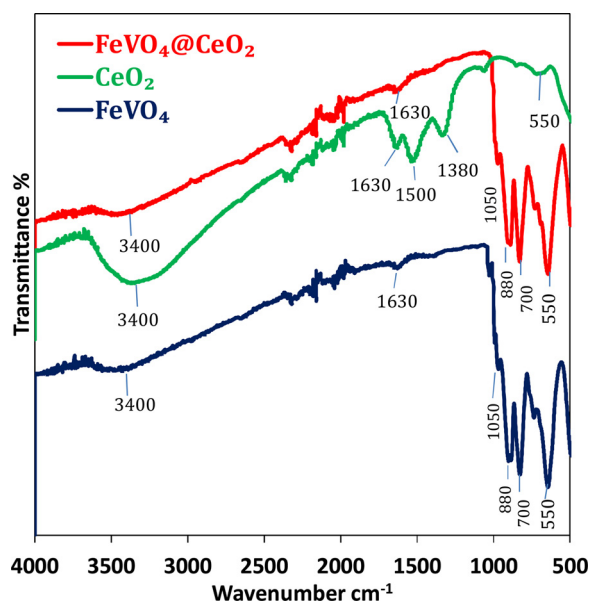
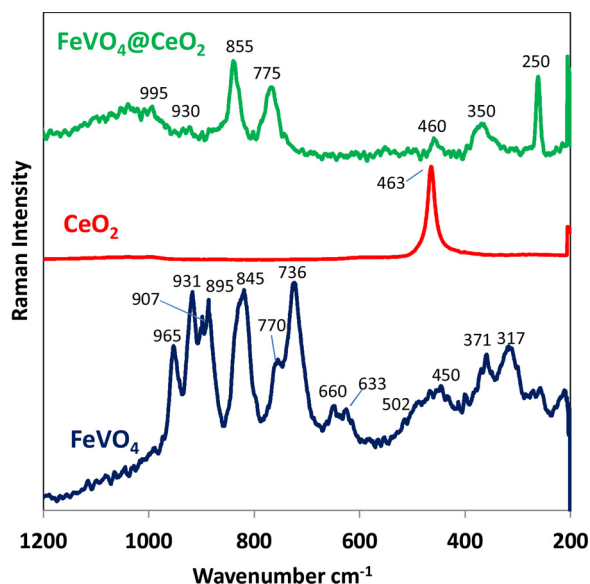
Fig. 4. FTIR spectra of FeVO₄, CeO₂ and FeVO₄@CeO₂.Fig. 5. Raman spectra of FeVO₄, CeO₂, and FeVO₄@CeO₂.

Table 1

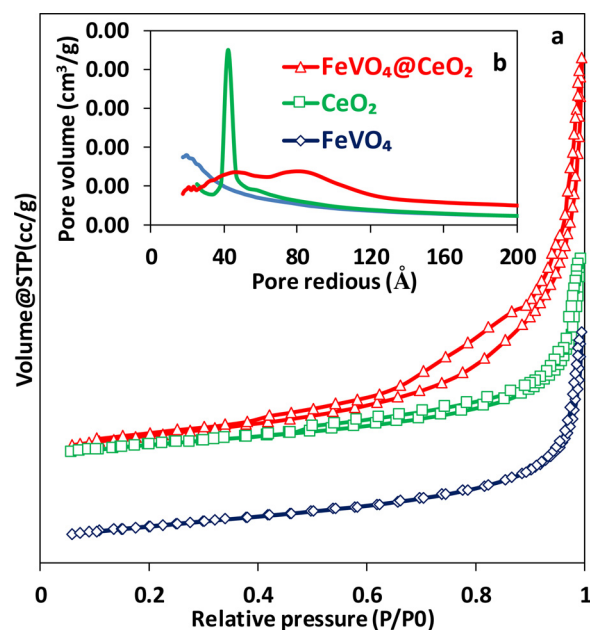
Textural data of FeVO₄, CeO₂ and FeVO₄@CeO₂.

Sample	S_{BET} (m ² /g)	V_p (m ³ /g)	$r = V_p/S_{BET}$ (Å)
FeVO ₄	24.2	0.032	13.2
CeO ₂	20.5	0.032	15.5
FeVO ₄ @CeO ₂	27.5	0.062	22.5

number of active sites and enhance the reactant mass transfer.

3.1.7. DRS

UV-vis diffuse reflectance spectroscopy (DRS) was performed to obtain the light absorption properties of FeVO₄, CeO₂, and FeVO₄@CeO₂ in the range of 250–800 nm (Fig. 7(a)). The values of the band gap energy of FeVO₄, CeO₂, and FeVO₄@CeO₂ were determined to be 1.95, 2.76 and 1.91 eV, respectively, as shown in Fig. 7(a). It can be seen that the absorption edge of the FeVO₄@CeO₂ exhibits a shift

Fig. 6. N₂ adsorption-desorption isotherms of FeVO₄, CeO₂ and FeVO₄@CeO₂ (a) pore size distributions of FeVO₄, CeO₂ and FeVO₄@CeO₂ (the inset (b)).

toward the visible region with a band gap energy (E_g), lower than that of FeVO₄ and CeO₂ due to the heterojunction structure, and defect states induced by oxygen vacancies (Li et al., 2015b) that leads to the formation of Ce³⁺ from Ce⁴⁺. This increase in the amount of Ce³⁺ states leads to the formation of localised energy states, which are closer to the conduction band and thereby decreasing the band gap (Saranya et al., 2014). In addition, oxygen vacancies and Ce³⁺ form intermediate defect energy states in the band gap. These intermediate energy states lead to retarding in the direct transition of photoinduced electrons from the valence band (VB) to the conduction band (CB), which in turn narrows the band gap (Choudhury et al., 2014). The transition character of the absorption edge (direct or indirect) was evaluated by plotting the square and square root of absorption coefficient against energy and then determining the linear one and the one that deviates away from the straight line (Zhang et al., 2006). The data reveal that the absorption edge of all the samples is caused by indirect transitions as shown in Fig. 7(b).

3.1.8. XPS

The composition and valance states of FeVO₄@CeO₂ were investigated by XPS analysis, the results of which are presented in Fig. 8(a), (b). The XPS patterns of FeVO₄@CeO₂ before sonophotocatalytic treatment are shown in Fig. 8(a). The survey XPS spectrum of FeVO₄@CeO₂ is composed primarily of peaks from C, Fe, O, V, and Ce. The C 1s peak at about 284.5 eV is attributed to the signal from carbon in the instrument and was used for calibration (Tomova et al., 2015). The peaks at 723.65 and 710.4 eV correspond to the Fe 2p_{1/2} and Fe 2p_{3/2} signals of Fe³⁺ species (Balamurugan et al., 2017). It can be clearly seen that the doublet peaks located at V 2p_{1/2} and 2p_{3/2} peaks at 525.2 and 516.9 eV, respectively, are attributed to V⁵⁺ in FeVO₄ (Yang et al., 2015), and the peak for O 1s located at about 531.77 eV is due to the formation of O–H bonds (Futsuhara et al., 1998). Two main peaks attributed to Ce⁴⁺ 3d_{5/2} and Ce⁴⁺ 3d_{3/2} are observed at the binding energies of 898.57 and 916.85 eV, respectively (Tsunekawa et al., 2000). The presence of Ce³⁺ 3d_{5/2} is observed at 882.73 eV. In addition to these, two peaks are observed at 890.45 and 908.89 eV, corresponding to the presence of Ce³⁺ 3d_{5/2} and Ce³⁺ 3d_{3/2}, respectively (Krishnamoorthy et al., 2014b). These results reveal the formation of a mixed valence state of cerium species of Ce³⁺ and Ce⁴⁺ in the FeVO₄@CeO₂. Moreover, the increase of Ce³⁺ species increases the

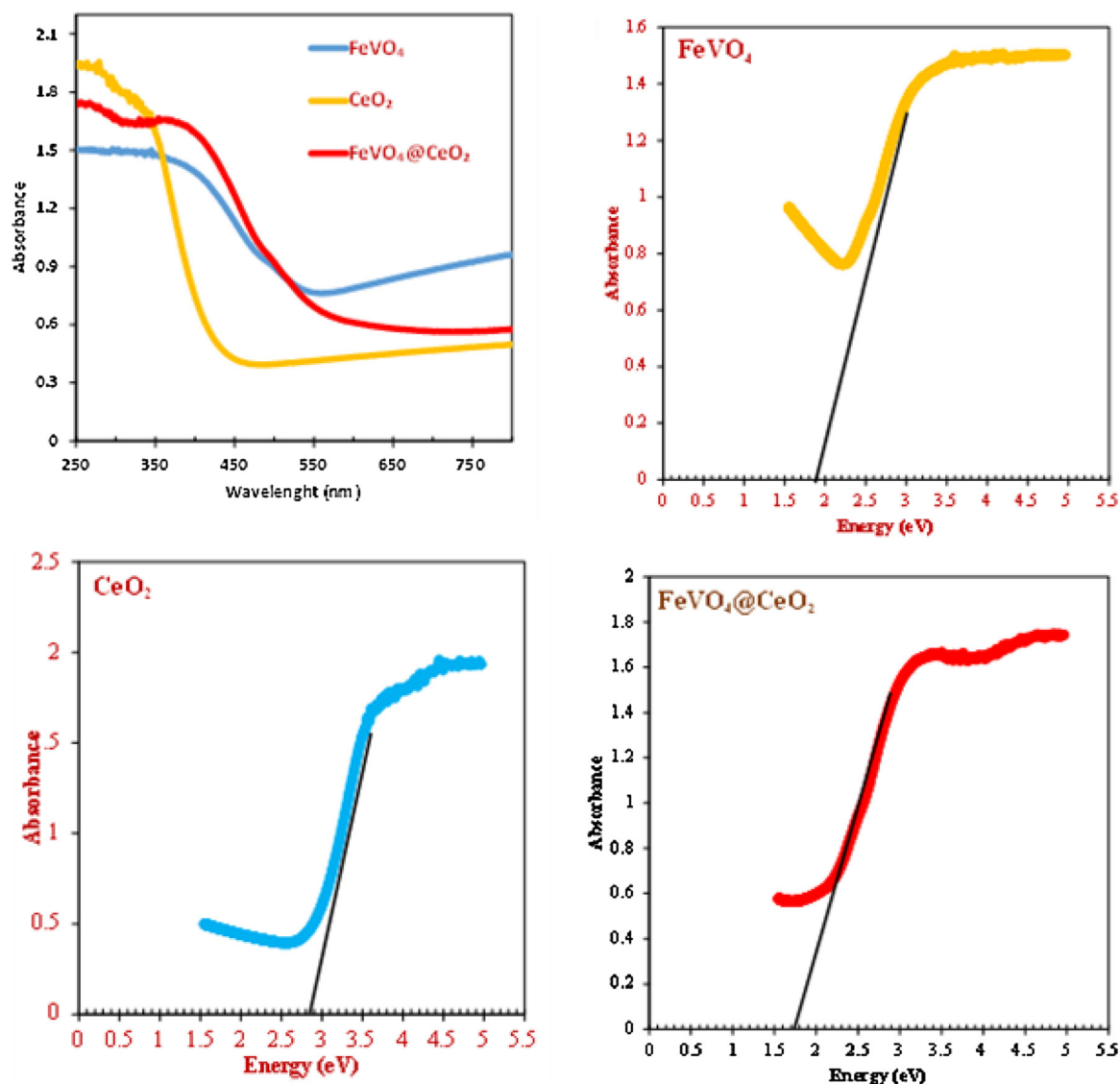


Fig. 7. (a). UV – vis DRS spectra of FeVO₄, CeO₂ and FeVO₄@CeO₂ and their band gap energies (b) Plots of $(\alpha h\nu)^2$ vs. energy and $(\alpha h\nu)^{1/2}$ vs. energy in the absorption edge region for FeVO₄, CeO₂ and FeVO₄@CeO₂.

oxygen vacancies around Ce⁴⁺, leading to the achievement of equilibrium charge in the catalysts (Guo et al., 2016). The above results demonstrate that FeVO₄@CeO₂ core shell is stable with the presence of Fe³⁺/Fe²⁺, V⁵⁺/V⁴⁺ and Ce³⁺/Ce⁴⁺ and can catalyse oxidation-reduction cycles in the presence of H₂O₂ to produce hydroxyl radicals. XPS spectra of FeVO₄@CeO₂ core shell nanoparticles after sonophotocatalytic treatment are shown in Fig. 8(b). The results demonstrate that there is no changes in the composition and valance states of the FeVO₄@CeO₂ in XPS spectra before and after sonophotocatalytic treatment but there are some obvious changes in the shape and in the intensity of the peaks which are related to the presence of Fe³⁺/Fe²⁺, V⁵⁺/V⁴⁺ and Ce³⁺/Ce⁴⁺ cycles in FeVO₄@CeO₂/H₂O₂ process. These changes reveal that hydroxyl radicals generated under heterogeneous Fenton like mechanism as described in Eqs. (1–6).

3.2. Insights in degradation of 4-NP using ultrasonic or ultraviolet irradiations in the presence of FeVO₄@CeO₂

3.2.1. Effect of sonolysis or photolysis conditions

To investigate the capability of (US) irradiation and (UV) irradiation on the degradation of 4-NP, the sonolysis and photolysis of 4-NP solutions were carried out in the absence of any oxidant or catalyst as

shown in Fig.S1. The obtained results revealed that the degradation extent reached 16% and 27% after 1 h of sonolysis and photolysis, respectively. This degradation capability can be ascribed to the generation of different free radicals (Petrier et al., 1994; Henglein, 1995) as a result of the photolysis or sonolysis of 4-NP aqueous solutions. The effect of H₂O₂ concentration on the sonolysis and photolysis of 4-NP was tested in a range of 5–40 mM Fig.S2. The addition of H₂O₂ enhanced the degradation performance of the sonolysis and photolysis of 4-NP reaching 38% and 50%, respectively, up to 20 mM H₂O₂, and after this concentration the degradation efficiency declined. This enhanced performance attributed to the production of extra amounts of free radicals and also because the ultrasonic-assisted cleavage of the O–O bond in H₂O₂ is much easier than O–H bond in water (Mehrdad and Hashemzadeh, 2010). However, the use of the extravagant H₂O₂ scavenges the free radicals generated instead of generating additional radicals (Abbasi and Asl, 2008).

3.2.2. Optimisation of ultrasonic or photo-heterogeneous Fenton

In the absence of any irradiation (US or UV), called (silent mode), several catalytic runs were performed. It has been observed that the extent of degradation was only 9% for 4-NP (20 ppm) using 40 mM H₂O₂, 0.1 g of the catalyst and pH 7 with continuous stirring for 1 h.

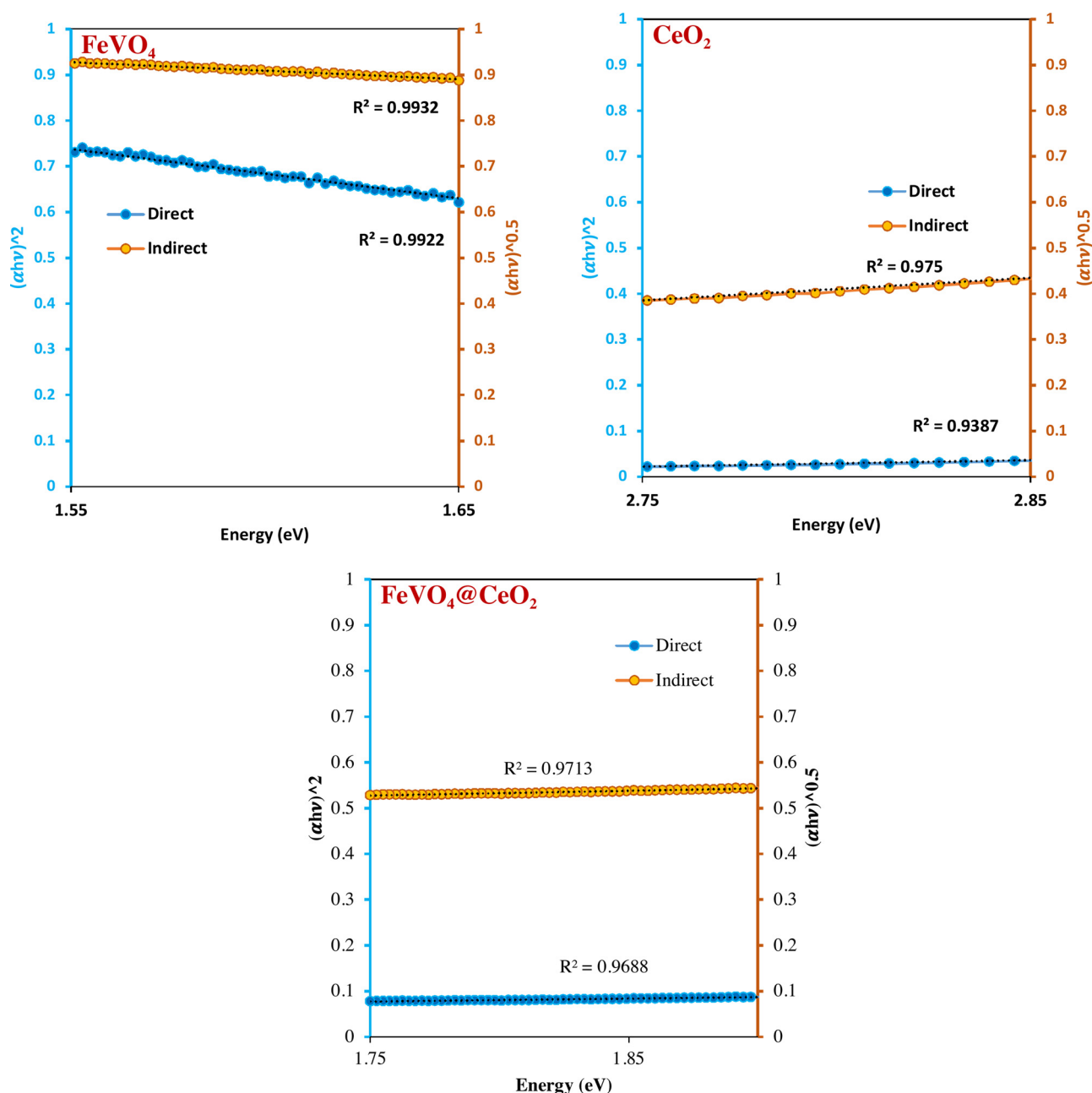
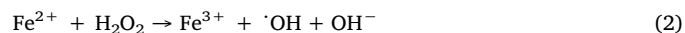
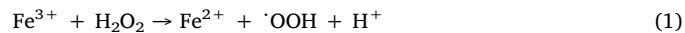


Fig. 7. (continued)

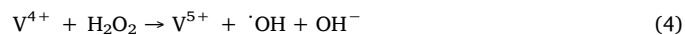
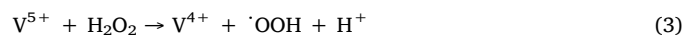
3.2.2.1. Optimisation of sonocatalytic or photocatalytic irradiation time. The FeVO₄@CeO₂ was introduced as heterogeneous Fenton like to the sonolysis or photolysis systems in the presence of H₂O₂ to enhance the degradation performance of the systems. The effect of irradiation time was investigated and the obtained data are presented in Fig. S3. The results demonstrate that using 0.1 g L⁻¹ of FeVO₄@CeO₂, 10 mM of H₂O₂, 4-NP (20 ppm), pH 7 and 1 h time for irradiation, a degradation extent of 85% and 94% was achieved for sonocatalytic or photocatalytic irradiation respectively.

3.2.2.1.1. Mechanistic insights into the sonocatalytic degradation of 4-NP over FeVO₄@CeO₂. To gain a full understanding of the sonocatalysis mechanism of 4-NP over the FeVO₄@CeO₂, the mechanism of Fenton-like reaction was studied. The catalytic mechanism possibly involved, in a special three-way Fenton-like mechanism, the dissociation of H₂O₂ by both Fe³⁺ and V⁵⁺ in FeVO₄ as the first and second pathway and Ce⁴⁺ in CeO₂ as the third pathway. The Fe³⁺ ions are able to react with H₂O₂ to generate an intermediate complex (Fe–O₂H₂⁺) that can be

dissociated into Fe²⁺ and HO₂[·] under (US) irradiation. Fe²⁺ ions are able to react with H₂O₂ to generate a higher concentration of [·]OH. The first pathway of the Fenton-like reaction is illustrated as follows (Kwan and Voelker, 2003):



The activation of V⁵⁺ in FeVO₄ with H₂O₂ to generate [·]OH as the second pathway is described in the following Eq. (Khaliullin et al., 2005; Kozlov et al., 2005):



It should be noted that the recycling of Fe³⁺ from Fe²⁺ in Eq. (2) and V⁵⁺ from V⁴⁺ in Eq. (4) is much slower than the reactions in Eq. (1) and in Eq. (3), respectively. Thus, we believed that these two redox

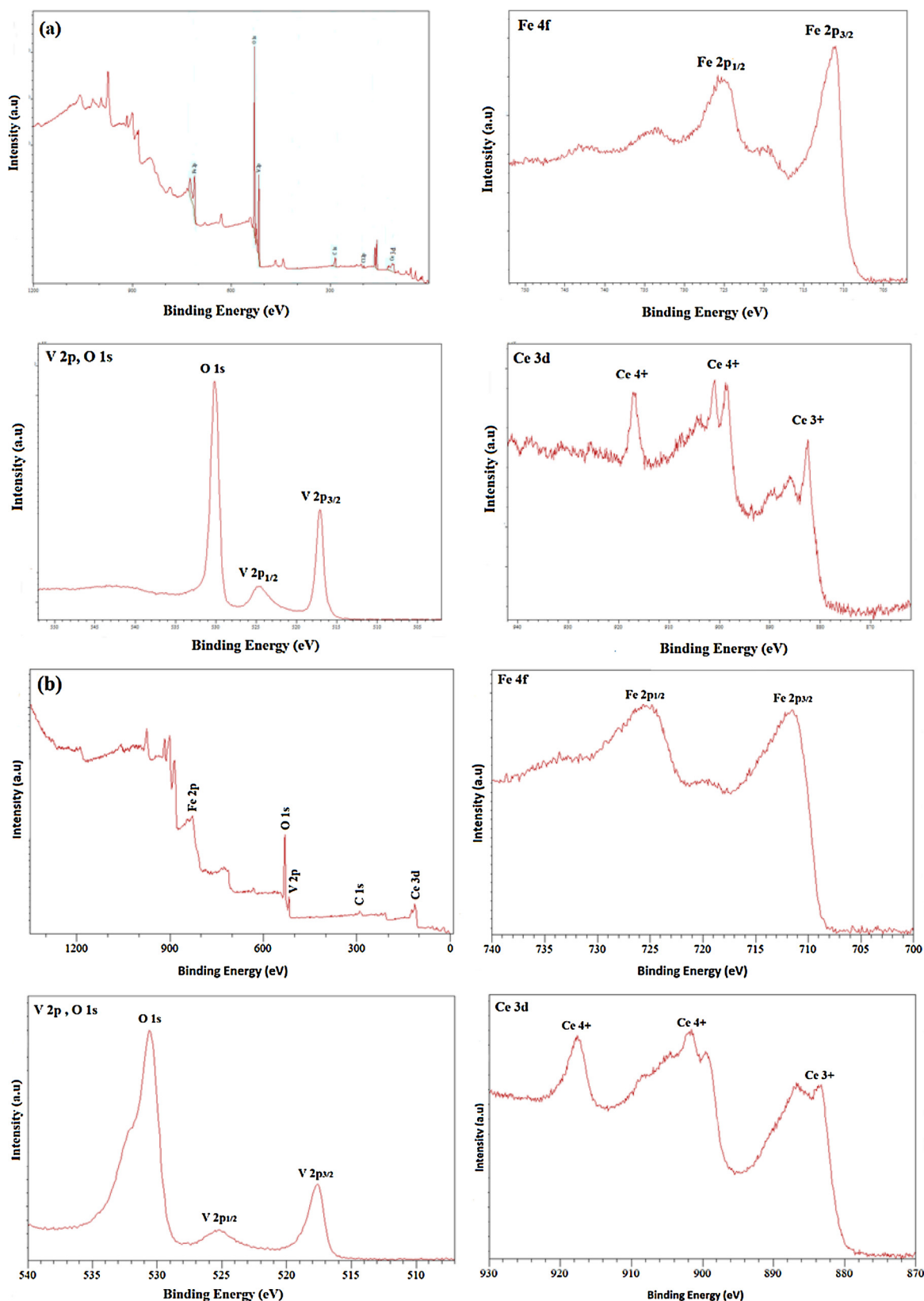
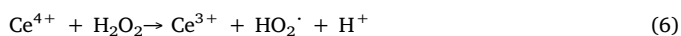


Fig. 8. XPS patterns of $\text{FeVO}_4@\text{CeO}_2$ (a) before and (b) after sonophotocatalytic treatment of the overall XPS survey, Fe 4f, V 2p, O 1s and Ce 3d.

cycles ($\text{Fe}^{3+}/\text{Fe}^{2+}$ and $\text{V}^{5+}/\text{V}^{4+}$) take place within the $\text{FeVO}_4\text{-H}_2\text{O}_2$ system. Furthermore, the redox cycle of CeO_2 between Ce^{3+} and Ce^{4+} as the third pathway makes it a potential candidate as a heterogeneous Fenton-like and thus can be employed efficiently in the degradation of

reluctant organic contaminants (Bokare and Choi, 2014). Heckert et al. (Heckert and Seal, 2008) reported that CeO_2 is able to generate considerable numbers of HO^\bullet in the presence of H_2O_2 as an oxidant, which is similar to that generated in an iron Fenton-like reaction according to

the following eqs. :



3.2.2.1.2. Mechanistic insights into photocatalytic degradation of 4-NP over FeVO₄@CeO₂. Based on the calculated band energy and data from the scavenging of the active species experiments above, a type-II staggered-gap type of heterojunction structure is formed between FeVO₄ and CeO₂ with tunable band edge potentials. The band edge positions for the semiconductor of both (CB) and (VB) at the value of PZC could be determined according to the following equations (Wetchakun et al., 2012; Huang et al., 2015):

$$E_{\text{CB}} = \chi - E_{\text{e}} - 1/2E_{\text{g}} \quad (7)$$

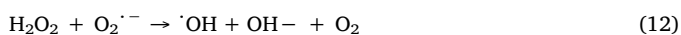
$$E_{\text{VB}} = E_{\text{g}} + E_{\text{CB}} \quad (8)$$

where χ represents the semiconductor's absolute electronegativity; E_{e} represents the free electrons energy on the hydrogen scale (ca. 4.5 eV); and E_{g} represents the semiconductor's band gap energy. The calculated values of both CB and VB of FeVO₄ are -0.44 and 1.56 eV, and those of CeO₂ are -0.32 and 2.44 eV, respectively. The possible mechanism was proposed under UV light irradiation; both FeVO₄ and CeO₂ can be activated since the VB and CB of CeO₂ are more negative than those calculated for FeVO₄. Thus, the excited electrons in the CB of CeO₂ transfer readily to the CB of FeVO₄. Also, the holes in the VB of FeVO₄ transfer directly to the VB of CeO₂. Such transitions in the heterojunction core-shell nanostructure afford substantial suppression in the e^-/h^+ pair recombination and also prolong the lifetime of the carriers. Moreover, this heterojunction structure in the presence of H₂O₂ can change the electronic structure and oxidation states of V^{4+}/V^{5+} and $\text{Ce}^{3+}/\text{Ce}^{4+}$. The V^{4+}/V^{5+} pairs are able to form energy state deficiency, which can act as an e^-/h^+ trap and thus suppress the rate of recombination (Luo et al., 2015). Moreover, the surface Ce^{4+} ions are able to trap the electrons in the CB where they are reduced to Ce^{3+} ions. These reduced ions (Ce^{3+}) are able to react with the dissolved oxygen to produce superoxide radicals (O_2^\cdot) and some of them may be re-oxidised again to Ce^{4+} using the generated holes or hydroxyl radicals to complete a cycle reaction. Thus, the existence of $\text{Ce}^{3+}/\text{Ce}^{4+}$ pairs not only effectively delays the e^-/h^+ pair recombination but also plays a role in the generation of O_2^\cdot (Jiang et al., 2016). Meanwhile, OH^\cdot are formed by oxidising the absorbed OH^- and H₂O using the holes in the VB of CeO₂ (Chen et al., 2016). Scheme 1 shows a mechanism of various radical generations over FeVO₄@CeO₂ core shell nanostructures in a sonophotocatalytic system for the degradation of 4-NP.

3.2.2.2. Optimisation of H₂O₂ concentration. To gain insight into the effects of H₂O₂ concentration on 4-NP degradation on FeVO₄@CeO₂, the addition of H₂O₂ in a range of 5–40 mM was examined. It was observed that an increase in sonocatalytic degradation and photocatalytic degradation of 4-NP in the range of 5 and 15 mM of H₂O₂ as shown in Fig.S4. It is obvious that, as the concentration of H₂O₂ increases, the extent of degradation of 4-NP increases up to an optimum concentration and then decreases. This is due to the scavenger effects of H₂O₂, which are illustrated by Eqs. (9) and (10) (Pham et al., 2018).



On the other hand, the addition of H₂O₂ also acts as an electron trap and is able to suppress the e^-/h^+ recombination (Malato et al., 2000), as can be described in Eq. (11) and (12):



3.2.2.3. Optimisation of catalyst amount. To unfold the role of catalyst amount on the degradation of 4-NP, different catalyst amounts in the range of 0.05–1 g L⁻¹ of FeVO₄@CeO₂ were tested as shown in Fig.S5 for (US) and (UV) irradiation. The obtained results revealed that, as the amounts of catalyst increases, the degradation efficiency increases up to 0.3 g L⁻¹ for (UV) and (US) irradiation and then begin to decrease slowly with a further increase in the catalyst amount. Due to the increase in the number of obtainable active sites, induces H₂O₂ decomposition and enhances the generation rate of cavitation bubbles and subsequently generates more hydroxyl radicals (Pham and Kim, 2018; ElMetwally et al., 2019). On the other hand, the decrease in the degradation efficiency by increasing the amount of the catalyst can be ascribed to the dissipation of the (US) irradiation by the agglomerated catalyst, (Pang and Abdullah, 2013; Pang et al., 2011) and also prevents the (UV) irradiation from illuminating the catalyst particles (Verma et al., 2013).

3.3. Optimisation of the sonophotocatalytic degradation of 4-NP using FeVO₄@CeO₂

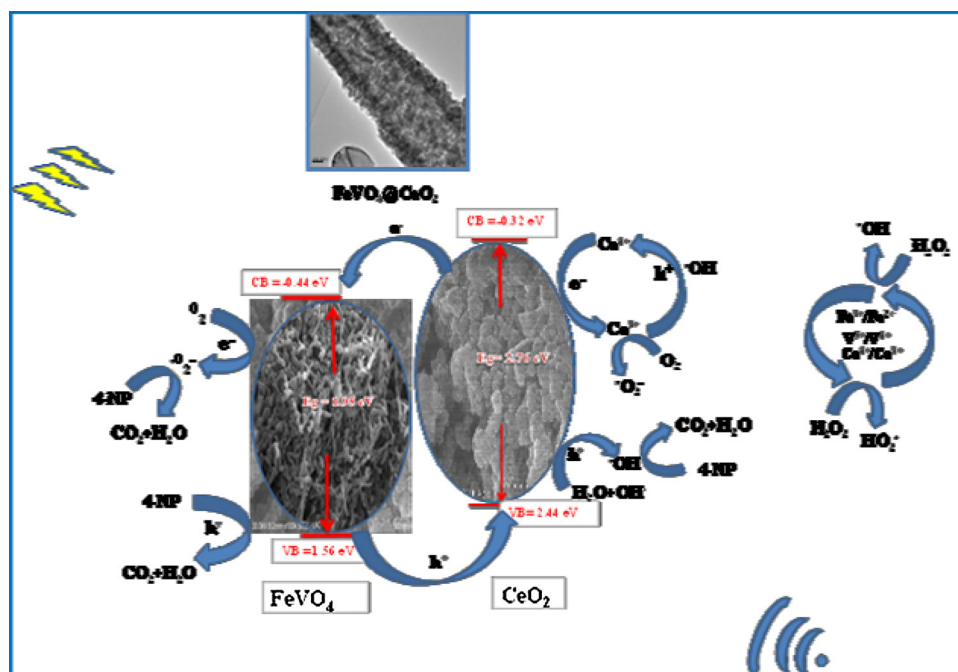
All the optimised conditions of the sonocatalytic and photocatalytic reactions were carefully selected and applied in the sonophoto-catalytic system as demonstrated in Fig. 9. The obtained results revealed that 30 min of binary irradiation US/UV was sufficient to complete the degradation of 4-NP (20 ppm) using 0.1 g L⁻¹ of FeVO₄@CeO₂ in the presence of 10 mM H₂O₂ at pH = 7. It is obvious that the degradation efficiency of the sonophotocatalytic system was higher than that of the sole sonocatalytic or photocatalytic system by 26% and 13%, respectively, following an order: sonophotocatalytic > photocatalytic > sonocatalytic performance. This remarkable performance can be ascribed to the ability of the US/UV system to exclude all the disadvantages observed in the individual systems, such as the blocking of the catalyst active sites, mass transfer limitations and catalyst fouling (Gogate and Pandit, 2004). The sonophotocatalytic degradation of 4-NP follows the pseudo first order and the obtained degradation rate for the US/UV system is found to be higher than the sum of the degradation rates of each systems under the same conditions as shown in Table 2 and Fig.S6. To obtain more precise results, the synergistic effect of sonophotocatalytic system, sonocatalysis and photocatalysis degradation of 4-NP was calculated by Eq. (13) (Verma et al., 2013).

$$\text{Synergy}(\%) = \frac{k_{\text{Sonophotocatalysis}} - (K_{\text{Sonocatalysis}} + K_{\text{Photocatalysis}})}{K_{\text{Sonophotocatalysis}}} \times 100$$

The data obtained from Table 2 show that the synergetic effect of US/UV system is faster than the sole systems and has a positive effect on 4-NP degradation performance

3.3.1. Optimisation of initial pH

To investigate the effect of initial pH on the sonophotocatalytic system, a wide pH range of 2.7–11 was screened as shown in Fig.S7. The obtained results revealed that the system was able to completely degrade 4-NP at the different pH values and even within the alkaline pH range after only 30 min of binary irradiation using FeVO₄@CeO₂. This remarkable performance shows that the working pH range of FeVO₄@CeO₂ can be extended to cover the alkaline pH range (pH = 9). The pKa of 4-NP is 7.15, so it is positively charged at below pH 9 and negatively charged at above pH 9 (Ahn et al., 2007). Augugliaro et al. (1993) reported that the photocatalytic degradation of 4-NP in the presence of TiO₂ decreased by increasing of the solution pH because the negatively charged TiO₂ particles repel the negatively charged 4-NP molecules, which in turn suppress photocatalytic performance. However, using FeVO₄@CeO₂ within the alkaline pH range, the degradation capability of the system was not reduced. This can be attributed to the presence of V^{5+} ion within FeVO₄, which is deemed a Lewis acid that is able to adsorb OH⁻ in the solution and alter the pH of the system



Scheme 1. Mechanism of various radicals generation over $\text{FeVO}_4@\text{CeO}_2$ core shell nanostructures in a sonophotocatalytic system for the degradation of 4-NP.

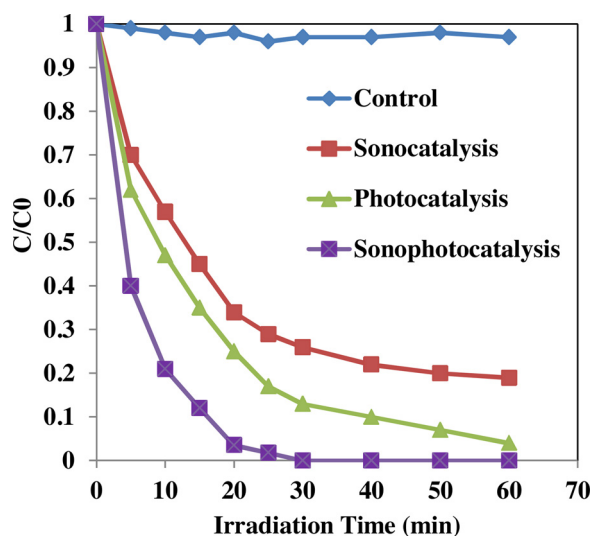


Fig. 9. Effect of irradiation time on sonocatalytic, photocatalytic and sonophotocatalytic degradation of 4-NP (20 ppm) in the presence of $\text{FeVO}_4@\text{CeO}_2$ (0.1 g L^{-1}), H_2O_2 (10 mM) at pH (7), and 25°C .

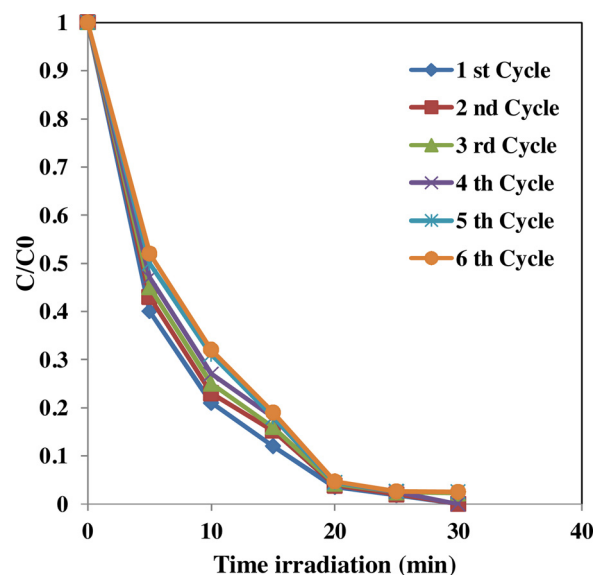


Fig. 10. Cycling runs of sonophotocatalytic degradation of 4-NP over $\text{FeVO}_4@\text{CeO}_2$ under optimum conditions.

(Rossetti et al., 2009; Ou et al., 2018). To further explain this outstanding phenomenon with the alkaline pH, the PZCs of the prepared samples were estimated using the mass titration method Fig.S8. The the PZC of $\text{FeVO}_4@\text{CeO}_2$ is higher than those of FeVO_4 and CeO_2 with values of 9.8, 8.1 and 8.2, respectively. This means that $\text{FeVO}_4@\text{CeO}_2$ particles remain positively charged up to pH 10, so the positively charged $\text{FeVO}_4@\text{CeO}_2$ particles will be able to attract the negatively

charged 4-NP molecules at the alkaline pH. This remarkable enhancement in the PZC value can be ascribed to the presence of Ce^{3+} ions that induces more defects in FeVO_4 crystals. The presence of such defects enhances the adsorption of hydroxyl species on the particles surface and then increases the affinity towards protons, which in turn increases the value of PZC (Deiana et al., 2010). The enhanced PZC reveals that the surface of the catalyst is highly susceptible to be positively charged, and

Table 2

Pseudo first order rate constants of 4-NP over $\text{FeVO}_4@\text{CeO}_2$.

Catalyst	Kus + uv + heterogeneous Fenton (min^{-1})	Kus + heterogeneous Fenton (min^{-1})	Kuv + heterogeneous Fenton (min^{-1})	Synergy	Synergy (%)
$\text{FeVO}_4@\text{CeO}_2$ core shell nanostructures	0.163	0.0472	0.0684	0.289	28.9%

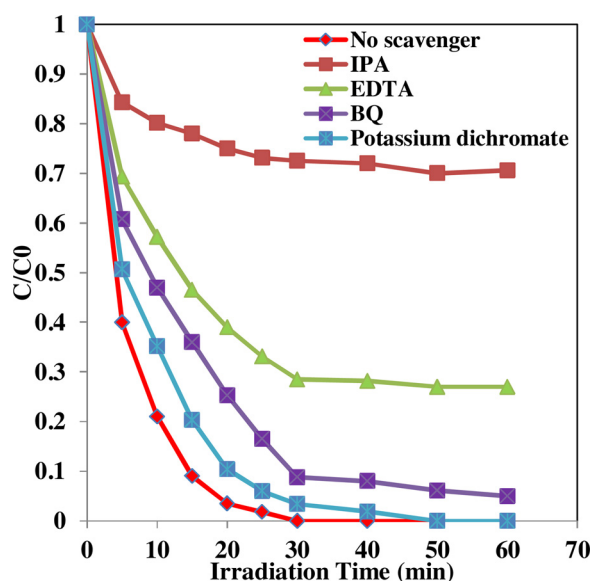


Fig. 11. Trapping experiments using different active species trappers for sonophotocatalytic degradation of 4-NP over $\text{FeVO}_4/\text{CeO}_2$.

so attracting the negatively charged molecules (Chai et al., 2013; Mohapatra et al., 2006).

3.4. Reusability

The sonophotocatalytic stability and reusability of $\text{FeVO}_4/\text{CeO}_2$ was investigated throughout six successive cycles under the same operating conditions Fig. 10. The sonophotocatalytic performance slightly decreased after six cycles. The synergic effect between FeVO_4 core and CeO_2 shell (Fig. 7 (a, b)) can enhance stability toward 4-NP degradation. Furthermore, to identify the change in the structure and morphological stability, the XRD after the first and sixth runs and the SEM of $\text{FeVO}_4/\text{CeO}_2$ after six runs were scrutinised Fig.S9 and Fig.S10.

3.5. TOC and mineralisation

The mineralisation performances of the materials, TOC analyses, were examined Fig.S11. $\text{FeVO}_4/\text{CeO}_2$ sonophotocatalyst possesses a high mineralisation capacity for the removal of 4-NP, reaching 92.2% in 30 min. The remarkable achievement of the sonophotocatalytic performance of the $\text{FeVO}_4/\text{CeO}_2$ can be attributed to its high adsorption rate, fast mass diffusion and enhanced performance of electron-holes pairs with a high generation rate of hydroxyl and superoxide radicals. The formed intermediates need longer time degrade completely, due to their slower rate of reaction with hydroxyl radicals attacking (Wang et al., 1998).

3.6. Radical scavengers

The pathway of the 4-NP sonophotocatalytic degradation by radical trapping was executed to investigate the main active species in the reaction Fig. 11. In this study, isopropanol (40 mmol L^{-1}), ethylene diamine tetraacetic acid (40 mmol L^{-1}), benzoquinone (4 mmol L^{-1}), and potassium dichromate (2 mmol L^{-1}) were used to trap hydroxyl radicals ($\cdot\text{OH}$), holes (h^+), superoxide radicals ($\text{O}_2^{\cdot-}$) and electron (e^-), respectively. The sonophotocatalytic performance is greatly inhibited with a slight difference by adding IPA, EDTA and BQ in comparison with the initial activity in the absence of radical scavengers, and follows the order $\cdot\text{OH} > h^+ > \text{O}_2^{\cdot-}$. On the other hand, the degradation performance is highly enhanced by adding potassium dichromate, which acts as a trapping agent for the generated electrons

and thus extends the lifetime of the holes.

4. Conclusions

Core shell nanostructured $\text{FeVO}_4/\text{CeO}_2$ acted as effective Fenton-like achieve high performance in the sonophotocatalytic degradation of 4-NP at low concentrations of the catalyst and oxidant. The synergistic effect of $\text{FeVO}_4/\text{CeO}_2$ enlarges the photoactivity of FeVO_4 and effectively inhibits the charge carrier recombination, ultimately improving the photocatalytic activity of FeVO_4 with CeO_2 . The hydroxyl radicals ($\cdot\text{OH}$) and holes (h^+) play a more important role than that of super oxide radicals ($\text{O}_2^{\cdot-}$) in the degradation process. This paper therefore opens up the prospect of further exploration of novel and interesting core-shell nanostructures for environmental remediation.

Acknowledgements

The authors wish to acknowledge the financial support of this research by Department of Green Chemistry, School of Engineering Science, LUT University, Mikkeli, Finland.

References

- Abbasi, M., Asl, N.R., 2008. Sonochemical degradation of Basic Blue 41 dye assisted by TiO_2 and H_2O_2 . *J. Hazard. Mater.* 153 (3), 942–947.
- Ahn, W.-Y., Sheeley, S.A., Rajh, T., Cropek, D.M., 2007. Photocatalytic reduction of 4-nitrophenol with arginine-modified titanium dioxide nanoparticles. *Appl. Catal. B: Environ.* 74 (1–2), 103–110.
- Ansari, A.A., Solanki, P.R., Malhotra, B.D., 2009. Hydrogen peroxide sensor based on horse radish peroxidase immobilised nanostructured cerium oxide film. *J. Biotechnol.* 142 (2), 179–184.
- Augugliaro, V., Lopezmunoz, M.J., Palmisano, L., Soria, J., 1993. Influence of pH on the degradation kinetics of nitrophenol isomers in a heterogeneous photocatalytic system. *Appl. Catal. A Gen.* 101 (1), 7–13.
- Bagal, M.V., Gogate, P.R., 2014. Wastewater treatment using hybrid treatment schemes based on cavitation and Fenton chemistry: a review. *Ultrason. Sonochem.* 21 (1), 1–14.
- Balamurugan, M., Yun, G., Ahn, K.-S., Kang, S.H., 2017. Revealing the beneficial effects of FeVO_4 nanoshell layer on the BiVO_4 inverse opal core layer for photoelectrochemical water oxidation. *J. Phys. Chem. C* 121 (14), 7625–7634.
- Bokare, A.D., Choi, W., 2014. Review of iron-free Fenton-like systems for activating H_2O_2 in advanced oxidation processes. *J. Hazard. Mater.* 275 (8), 121–135.
- Cao, J., Xu, B., Lin, H., Luo, B., Chen, S., 2012. Chemical etching preparation of BiOI/BiOBr heterostructures with enhanced photocatalytic properties for organic dye removal. *J. Chem. Eng.* 185–186 (10), 91–99.
- Cargnello, M., Wieder, N., Montini, T., Gorte, R., Fornasiero, P., 2010. Synthesis of dispersible Pd/CeO_2 core-shell nanostructures by self-assembly. *J. Am. Chem. Soc.* 132 (4), 1402–1409.
- Chae, B.W., Amna, T., Hassan, M.S., Al-Deyab, S.S., Khil, M.S., 2017. $\text{CeO}_2/\text{Cu}_2\text{O}$ composite nanofibers: synthesis, characterisation photocatalytic and electrochemical application. *Adv. Powder Technol.* 28 (1), 230–235.
- Chai, L., Wang, Y., Zhao, N., Yang, W., You, X., 2013. Sulfate-doped $\text{Fe}_3\text{O}_4/\text{Al}_2\text{O}_3$ nanoparticles as a novel adsorbent for fluoride removal from drinking water. *Water Res.* 47 (12), 4040–4049.
- Chen, F., Ho, P., Ran, R., Chen, W., Si, Z., Wu, X., Weng, D., Huang, Z., Lee, C., 2017. Synergistic effect of CeO_2 modified TiO_2 photocatalyst on the enhancement of visible light photocatalytic performance. *J. Alloy. Compd.* 714 (15), 560–566.
- Chen, L., Meng, D., Wu, X., Wang, A., Wang, J., Wang, Y., Yu, M., 2016. In situ synthesis of V^{4+} and Ce^{3+} self-doped $\text{BiVO}_4/\text{CeO}_2$ heterostructured nanocomposites with high surface areas and enhanced visible-light photocatalytic activity. *J. Phys. Chem. C* 120 (33), 18548–18559.
- Chilukoti, B.S., Vijayanand, M., Aniruddha, B.P., Muthupandian, A., 2011. Mechanistic investigations on sonophotocatalytic degradation of textile dyes with surface active solutes. *Ind. Eng. Chem. Res.* 50 (20), 11485–11494.
- Choudhury, B., Chetri, P., Choudhury, A., 2014. Oxygen defects and formation of Ce^{3+} affecting the photocatalytic performance of CeO_2 Nanoparticles. *RSC Adv.* 4 (9), 4663–4671.
- Deiana, C., Fois, E., Coluccia, S., Martra, G., 2010. Surface structure of TiO_2 P25 nanoparticles: infrared study of hydroxy groups on coordinative defect sites. *J. Phys. Chem. C* 114 (49), 21531–21538.
- Ding, M., Yao, N., Wang, C., Huang, J., Shao, M., Zhang, S., Li, P., Deng, X., Xu, X., 2016. ZnO/CdS core-shell heterostructures: fabrication, enhanced photocatalytic, and photoelectrochemical performance. *Nanoscale Res. Lett.* 11 (1), 205–211.
- ElMetwally, A.E., Eshaq, G., Al-Sabagh, A.M., Yehia, F.Z., Philip, C.A., Moussa, N.A., ElShafei, G.M.S., 2019. Insight into heterogeneous Fenton-sonophotocatalytic degradation of nitrobenzene using metal oxychlorides. *Sep. Purif. Technol.* 210 (36), 452–462.
- ElShafei, G.M.S., Al-Sabagh, A.M., Yehia, F.Z., Philip, C.A., Moussa, N.A., Eshaq, G., ElMetwally, A.E., 2018. Metal oxychlorides as robust heterogeneous Fenton catalysts

- for the sonophotocatalytic degradation of 2-nitrophenol. *Appl. Catal. B Environ.* 224 (28), 681–691.
- Erick, R.B., Dolores, M., Evaristo, M., Dionysios, D., 2004. Degradation of microcystin-LR, toxin by Fenton and Photo-Fenton processes. *Toxicol.* 43 (7), 829–832.
- Fan, Z., Meng, F., Gong, J., Li, H., Hu, Y., Liu, D., 2016. Enhanced photocatalytic activity of hierarchical flower-like $\text{CeO}_2/\text{TiO}_2$ heterostructures. *Mater. Lett.* 175 (7), 36–39.
- Franca, A.S., Oliveira, L.S., Ferreira, M.E., 2009. Kinetics and equilibrium studies of methylene blue adsorption by spent coffee grounds. *Desalination*. 249 (1), 267–272.
- Futsuhara, M., Yoshioka, K., Takai, O., 1998. Optical properties of zinc oxynitride thin films. *Thin Solid Films* 317 (1), 322–325.
- Ghows, N., Entezari, M., 2012. Sono-synthesis of core-shell nanocrystal (CdS/TiO_2) without surfactant. *Ultrason. Sonochem.* 19 (5), 1070–1078.
- Gogate, P.R., 2008. Treatment of wastewater streams containing phenolic compounds using hybrid techniques based on cavitation: a review of Current Status and the way forward. *Ultrason. Sonochem.* 15 (1), 1–15.
- Gogate, P.R., Pandit, A.B., 2004. Sonophotocatalytic reactors for wastewater treatment: a critical review. *AIChE J.* 50 (5), 1051–1079.
- Guo, X.L., Li, J., Zhou, R.X., 2016. Catalytic performance of manganese doped $\text{CuO}-\text{CeO}_2$ catalysts for selective oxidation of CO in hydrogen-rich gas. *Fuel* 163 (9), 56–64.
- Habila, M.A., AlOthman, Z.A., El-Toni, A.M., Labis, J.P., Soyak, M., 2016. Synthesis and application of $\text{Fe}_3\text{O}_4/\text{SiO}_2/\text{TiO}_2$ for photocatalytic decomposition of organic matrix simultaneously with magnetic solid phase extraction of heavy metals prior to ICP-MS analysis. *Talanta* 154 (23), 539–547.
- He, G.-H., He, G.-L., Li, A.-J., Li, X., Wang, X.-J., Fang, Y.-P., Xu, Y.-H., 2014. Synthesis and visible light photocatalytic behavior of WO_3 (core)/ Bi_2WO_6 (shell). *J. Mol. Catal. A Chem.* 385 (4), 106–111.
- Heckert, E.G., Seal, S.W.T., 2008. Self, Fenton-like reaction catalyzed by the rare earth inner transition metal cerium. *Environ. Sci. Technol.* 42 (13), 5014–5019.
- Henglein, A., 1995. Chemical effects of continuous and pulsed ultrasound in aqueous solutions. *Ultrason. Sonochem.* 2 (2), S115–S121.
- Herrera-Melián, J.A., Martín-Rodríguez, A.J., Ortega-Méndez, A., Araña, J., Doña-Rodríguez, J.M., Pérez-Peña, J., 2012. Degradation and detoxification of 4-nitrophenol by advanced oxidation technologies and bench-scale constructed wetlands. *J. Environ. Manage.* 105 (30), 53–60.
- Hosseinpour-Mashkani, S.M., Sobhani-Nasab, A., Maddahfar, M., 2016. Synthesis, characterisation and investigation magnetic and photovoltaic properties of FeVO_4 nanoparticles. *J. Nanostructure Chem.* 6 (1), 70–73.
- Hu, S., Zhou, F., Wang, L., Zhang, J., 2011. Preparation of $\text{Cu}_2\text{O}/\text{CeO}_2$ heterojunction photocatalyst for the degradation of Acid Orange 7 under visible light irradiation. *Catal. Commun.* 12 (9), 794–797.
- Huang, B., Yu, D., Sheng, Z., Yang, L., 2017. Novel $\text{CeO}_2/\text{TiO}_2$ core-shell nanostructure catalyst for selective catalytic reduction of NO_x with NH_3 . *J. Environ. Sci. China (China)* 55 (25), 129–136.
- Huang, H.W., Liu, L.Y., Zhang, Y.H., Tian, N., 2015. Novel $\text{BiVO}_4/\text{BiVO}_4$ Composite Photocatalyst with Highly Improved Visible-Light-Induced Photocatalytic Performance for Rhodamine B Degradation and Photocurrent Generation. *RSC Adv.* 5 (2), 1161–1167.
- Ijaz, S., Ehsan, M.F., Ashiq, M.N., Karamat, N., He, T., 2016. Preparation of CdS/CeO_2 core/shell composite for photocatalytic reduction of CO_2 under visible-light irradiation. *Appl. Surf. Sci.* 390 (20), 550–559.
- Jiang, Z., Liu, Y., Jing, T., Huang, B., Zhang, X., Qin, X., Dai, Y., Whangbo, M.-H., 2016. Enhancing the photocatalytic activity of BiVO_4 for oxygen evolution by Ce doping: Ce^{3+} ions as hole traps. *J. Phys. Chem. C* 120 (4), 2058–2063.
- Kaneti, Y., Zhang, Z., Yue, J., Jiang, X., Yu, A., 2013. Porous FeVO_4 nanorods: synthesis, characterisation, and gas-sensing properties toward volatile organic compounds. *J. Nanopart. Res.* 15 (8), 1948–1963.
- Kanmani, S.S., Ramachandran, K., 2012. Synthesis and characterisation of TiO_2/ZnO core/shell nanomaterials for solar cell applications. *Renew. Energy* 43 (C), 149–156.
- Khalilullin, R.Z., Bell, A.T., Head-Gordon, M., 2005. A density functional theory study of the mechanism of free radical generation in the system vanadate/ $\text{PCA}/\text{H}_2\text{O}_2$. *J. Phys. Chem. B* 109 (38), 17984–17992.
- Khanchandani, S., Kumar, S., Ashok, S.K., Ganguli, A.K., 2016. Comparative study of TiO_2/CuS Core/Shell and composite nanostructures for efficient visible light photocatalysis. *ACS Sustainable Chem. Eng.* 4 (3), 1487–1499.
- Khanchandani, S., Srivastava, P., Kumar, S., Ghosh, S., Ganguli, A., 2014. Band gap engineering of ZnO using Core/Shell morphology with environmentally benign Ag_2S sensitizer for efficient light harvesting and enhanced visible-light photocatalysis. *Inorg. Chem.* 53 (17), 8902–8912.
- Kozlov, Y.N., Nizova, G.V., Shul'pin, G.B., 2005. Oxidations by the reagent $\text{O}_2-\text{H}_2\text{O}_2$ vanadium derivative-pyrazine-2-carboxylic acid: part 14. Competitive oxidation of alkanes and acetonitrile (solvent). *J. Mol. Catal. A Chem.* 227 (1–2), 247–253.
- Krishnamoorthy, K., Veerapandian, M., Zhang, L.-H., Yun, K., Kim, S.J., 2014a. Surface chemistry of cerium oxide nanocubes: toxicity against pathogenic bacteria and their mechanistic study. *J. Ind. Eng. Chem.* 20 (5), 3513–3517.
- Krishnamoorthy, K., Veerapandian, M., Zhang, L.-H., Yun, K., Kim, S.J., 2014b. Surface chemistry of cerium oxide nanocubes: Toxicity against pathogenic bacteria and their mechanistic study. *J. Ind. Eng. Chem.* 20 (5), 3513–3517.
- Kwan, W.P., Voelker, B.M., 2003. Rates of hydroxyl radical generation and organic compound oxidation in mineral-catalyzed fenton-like systems. *Environ. Sci. Technol.* 37 (6), 1150–1158.
- Lehnen, T., Valldor, M., Nižňanský, D., Mathur, S., 2014. Hydrothermally grown porous FeVO_4 nanorods and their integration as active material in gas-sensing Devices. *Mater. Chem. A* 2 (6), 1862–1868.
- Li, S., Wang, F., Wang, S., Zhou, H., Li, H., 2015a. Synthesis of buckhorn-like BiVO_4 with a shell of CeO_2 nanodots: effect of heterojunction structure on the enhancement of photocatalytic activity. *Appl. Catal. B Environ.* 170 (7), 186–194.
- Li, K., Gao, S.M., Wang, Q.Y., Xu, H., Wang, Z.Y., Huang, B.B., Dai, Y., Lu, J., 2015b. In situ-Reduced synthesis of Ti^{3+} self-doped $\text{TiO}_2/\text{g-C}_3\text{N}_4$ heterojunctions with high photocatalytic performance under LED light irradiation. *ACS Appl. Mater. Interfaces* 7 (17), 9023–9030.
- Lunhong, Ai, Jing, J., 2013. Catalytic reduction of 4-nitrophenol by silver nanoparticles stabilised on environmentally benign macroscopic biopolymer hydrogel. *Short Communication. Bioresour. Technol.* 132 (22), 374–377.
- Luo, Z., Poyraz, A.S., Kuo, C.H., Miao, R., Meng, Y.T., Chen, S.Y., Jiang, T., Wenos, C., Suib, S.L., 2015. Crystalline mixed phase (Anatase/Rutile) mesoporous titanium dioxides for visible light photocatalytic activity. *Chem. Mater.* 27 (1), 6–17.
- Malato, S., Blanco, J., Maldonado, M., Fernández-Ibáñez, P., Campos, A., 2000. Optimising solar photocatalytic mineralisation of pesticides by adding inorganic oxidising species; application to the recycling of pesticide containers. *Appl. Catal. B Environ.* 28 (3–4), 163–174.
- Mehrdad, A., Hashemzadeh, R., 2010. Ultrasonic degradation of rhodamine B in the presence of hydrogen peroxide and some metal oxide. *Ultrason. Sonochem.* 17 (1), 168–172.
- Mishra, K.P., Gogate, P.R., 2011. Intensification of sonophotocatalytic degradation of p-nitrophenol at pilot scale capacity. *Ultrason. Sonochem.* 18 (3), 739–744.
- Mitsudome, T., Kaneda, K., 2013. Advanced core-shell nanoparticle catalysts for efficient organic transformations. *Chem. Cat. Chem.* 5 (7), 1681–1691.
- Mohapatra, M., Sahoo, S., Anand, S., Das, R., 2006. Removal of As (V) by Cu(II) -, Ni(II) -, or Co(II) -doped goethite samples. *J. Colloid Interface Sci.* 298 (1), 6–12.
- Nithya, V.D., Kalai Selvan, R., Sanjeeviraja, C., Mohan Radheep, D., Arumugam, S., 2011. Synthesis and characterisation of FeVO_4 nanoparticles. *Mar. Res. Bull.* 46 (10), 1654–1658.
- Ou, X., Yan, J., Zhang, F., Zhang, C., 2018. Accelerated degradation of orange G over a wide pH range in the presence of FeVO_4 . *Front. Environ. Sci. Eng. China* 12 (7), 1–7.
- Pang, Y.L., Abdullah, A.Z., 2013. Fe^{3+} doped TiO_2 nanotubes for combined adsorption-sonocatalytic degradation of real textile wastewater. *Appl. Catal. B* 129 (13), 473–481.
- Pang, Y.L., Abdullah, A.Z., Bhatia, S., 2011. Review on sonochemical methods in the presence of catalysts and chemical additives for treatment of organic pollutants in wastewater. *Desalination* 277 (1–3), 1–14.
- Peretz, S., Cinteza, O. Removal of some nitrophenol contaminants using alginate gel beads.
- Petrier, C., Lamy, M.-F., Francony, A., Benahcene, A., David, B., Renaudin, V., Gondrexon, N., 1994. Sonochemical degradation of phenol in dilute aqueous solutions: comparison of the reaction rates at 20 and 487 kHz. *J. Phys. Chem.* 98 (41), 10514–10520.
- Pham, V.L., Kim, S.K., 2018. $\text{Cu}/\text{Fe}_3\text{O}_4$ core-shell nanoparticle-catalyzed oxidative degradation of the antibiotic oxytetracycline in pre-treated landfill leachate. *Chemosphere* 191 (31), 639–650.
- Pham, V.L., Kim, D.-G., Ko, S.-O., 2018. Oxidative degradation of the antibiotic oxytetracycline by $\text{Cu}/\text{Fe}_3\text{O}_4$ core-shell nanoparticles. *Sci. Total Environ.* 631–632 (26), 608–618.
- Ricardo, A., Efraim, A., 2018. Advanced oxidation processes for waste water treatment. *Emerging Green Chemical Technology. Chapter 7 – Sonolysis* 177–213.
- Rossetti, I., Fabbri, L., Ballarín, N., Oliva, C., Cavani, F., Cericola, A., Bonelli, B., Piumetti, M., Garrone, E., Dyrbeck, H., Blekkan, E.A., Forni, L., 2009. V–Al–O catalysts prepared by flame pyrolysis for the oxidative dehydrogenation of propane to propylene. *Catal. Today* 141 (3–4), 271–281.
- Saranya, J., Ranjith, K.S., Saravanan, P., Mangalajaraj, D., Kumar, R., 2014. Cobalt-doped cerium oxide nanoparticles: enhanced photocatalytic activity under UV and visible light irradiation. *Mater. Sci. Semicond. Process.* 26 (99), 218–224.
- Shah, N.H., Bhangaonkar, K.R., Pinjari, D.V., Mhaske, S.T., 2016. Ultrasonically engineered ceria-titania nanostructure mediated photocatalytic and sonocatalytic degradation of organic dye. *Austin Chem Eng.* 3 (3), 1032–2016.
- Siadatnasab, S.F., Khataee, A., 2017. Ultrasound-assisted degradation of organic dyes over magnetic $\text{CoFe}_2\text{O}_4/\text{ZnS}$ core-shell nanocomposite. *Ultrason. Sonochem.* 37 (11), 298–309.
- Sing, K.S.W., Everett, D.H., Haul, R.A.W., Moscou, L., Pierotti, R.A., Rouquerol, J., Siemieniowska, T., 1985. Reporting Physicochemical data for Gas/Solid Systems with Special Reference to the determination of surface area and porosity. *Pure Appl. Chem.* 57 (4), 603–619.
- Slimane, M., Oualid, H., Fethi, S., Mahdi, C., 2010. Sonochemical degradation of Rhodamine B in aqueous phase: effects of additives. *Chem. Eng. J.* 158 (3), 550–557.
- Tomova, D., Iliev, V., Eliyas, A., Rakovsky, S., 2015. Promoting the oxidative removal rate of oxalic acid on gold-doped $\text{CeO}_2/\text{TiO}_2$ photocatalysts under UV and visible light irradiation. *Sep. Purif. Technol.* 156 (2), 715–723.
- Tsunekawa, S., Fukuda, T., Kasuya, A., 2000. X-ray photoelectron spectroscopy of monodispersed CeO_x nanoparticles. *Surf. Sci.* 457 (3), L437–L440.
- Verma, A., Kaur, H., Dixit, D., 2013. Photocatalytic, sonolytic and sonophotocatalytic degradation of 4-chloro-2-nitro phenol. *Arch. Environ. Prot* 39 (2), 17–28.
- Vuk, A., Orel, B., Draz'ic, G., 2001. IR spectroelectrochemical studies of $\text{Fe}_2\text{V}_4\text{O}_{13}$, FeVO_4 and InVO_4 thin films obtained via sol-gel synthesis. *J. Solid State Electrochem.* 5 (7–8), 437–449.
- Wang, K.-H., Hsieh, Y.-H., Chen, L.-J., 1998. The heterogeneous photocatalytic degradation intermediates and mineralisation for the aqueous solution of cresols and nitrophenols. *J. Hazard. Mater.* 59 (28), 251–260.
- Wetchakun, N., Chaiwichain, S., Inceesungvorn, B., Pingmuang, K., Phanichphant, S., Minett, A.L., Chen, J., 2012. $\text{BiVO}_4/\text{CeO}_2$ Nanocomposites with High Visible-Light-Induced Photocatalytic Activity. *ACS Appl. Mater. Interfaces* 4 (7), 3718–3723.
- Yang, W., Tan, G.Q., Huang, J., Ren, H.J., Xia, A., Zhao, C.C., 2015. Enhanced magnetic property and photocatalytic activity of UV-light responsive N-doped $\text{Fe}_2\text{O}_3/\text{FeVO}_4$ heterojunction. *Ceram. Int.* 41 (1), 1495–1503.
- Yehia, F.Z., Eshaq, G., ElMetwally, A.E., 2016. Enhancement of the working pH range for

- degradation of p-nitrophenol using Fe^{2+} -aspartate and Fe^{2+} -glutamate complexes as modified Fenton reagents. *Egypt. J. Pet* 25 (2), 239–245.
- Zaleska, A., Marchelek, M., Diak, M., Grabowska, E., 2016. Noble metal-based bimetallic nanoparticles: the effect of the structure on the optical, catalytic and photocatalytic properties. *Adv. Colloid Interf. Sci.* 229 (4), 80–107.
- Zhang, M., Sheng, Q., Nie, F., Zheng, J., 2014. Synthesis of Cu nanoparticles-loaded Fe_3O_4 @carbon core-shell nanocomposite and its application for electrochemical sensing of hydrogen peroxide. *J. Electroanal. Chem. Lausanne (Lausanne)* 730 (2), 10–15.
- Zhang, P., Liu, Y., Tian, B., Luo, Y., Zhang, J., 2017. Synthesis of core-shell structured CdS@CeO_2 and CdS@TiO_2 composites and comparison of their photocatalytic activities for the selective oxidation of benzyl alcohol to benzaldehyde. *Catal. Today* 281 (26), 181–188.
- Zhang, K.-L., Liu, C.-M., Huang, F.-Q., Zheng, C., Wang, W.-D., 2006. Study of the electronic structure and photocatalytic activity of the BiOCl photocatalyst. *Appl. Catal. B: Environ* 68 (3–4), 125–129.
- Zheng, X., Huang, M., You, Y., Peng, H., Wen, J., 2018a. Core-shell structured $\alpha\text{-Fe}_2\text{O}_3\text{@CeO}_2$ heterojunction for the enhanced visible-light photocatalytic activity. *Mater. Res. Bull.* 101 (12), 20–28.
- Zheng, X., Huang, M., You, Y., Peng, H., Wen, J., 2018b. Core-shell structured $\alpha\text{-Fe}_2\text{O}_3\text{@CeO}_2$ heterojunction for the enhanced visible-light photocatalytic activity. *Mater. Res. Bull.* 101 (12), 20–28.